Nanotransfer Printing for Synthesis of Vertically Aligned Carbon Nanotubes with Enhanced Atomic Penetration

Ji-Hwan Ha[§], Inyeong Yang[§], Junseong Ahn[§], Sukkyung Kang, Zhi-Jun Zhao, Yongrok Jeong, Hyeongmin Je, Joono Cheong, Soon Hyoung Hwang, Sohee Jeon, Jun-Ho Jeong[*], Sanha Kim[*], and Inkyu Park[*]

J.-H Ha, I. Yang, S. Kang, H. Je, S. Kim, and I. Park
Department of Mechanical Engineering, Korea Advanced Institute of Science and Technology, Daejeon 34141, Republic of Korea.
E-mail: E-mail address: Sanhkim@kaist.ac.kr; ORCID: https://orcid.org/0000-0002-3548-6173; inkyu@kaist.ac.kr; ORCID: https://orcid.org/0000-0001-5761-7739.

J. Ahn, J. Cheong
Department of Electro-Mechanical Systems Engineering, Korea University, Sejong, 30019 Republic of Korea

S. H. Hwang, S. Jeon, J.-H. Jeong
Department of Nano-manufacturing Technology, Korea Institute of Machinery and Materials, Daejeon 34103, Republic of Korea.
E-mail: jhjeong@kimm.re.kr; ORCID: https://orcid.org/0000-0003-0671-0225.

Z.-J. Zhao
Institute of Smart City and Intelligent Transportation, Southwest Jiaotong University, Chengdu 611756, China.

Y. Jeong
Radioisotope Research Division, Korea Atomic Energy Research Institute, Daejeon, 34057, Republic of Korea

[§]These authors contributed equally to the work.

Keywords: nanopatterning, vertically aligned carbon nanotubes, atomic layer deposited VACNT, VACNT-based gas sensor, atomic penetration

Vertically aligned carbon nanotubes (VACNTs) exhibit outstanding mechanical strength, chemical stability, and electrical characteristics; however, their constrained mechanical elasticity and chemical responsiveness spurred research on atomic decoration techniques for enhancing their mechanochemical attributes. Nevertheless, achieving uniform atomic decoration on the VACNT surface is difficult because of the high density and large aspect ratio of VACNT. Herein, a strategy to design and apply nanopatterned VACNTs (nVACNTs) based on a nanotransfer printing process is proposed to improve atomic penetrability. Nanopatterns inherent to nVACNTs facilitate atomic penetration, allowing for the more consistent and higher quality deposition of functional materials such as zinc oxide and alumina by atomic layer deposition. Furthermore, physical vapor deposition provides an improved coating of metal catalyst such as gold. The uniform deposition of ceramic layers on the entire surface of nVACNTs strengthen its mechanical resilience, owing to the diminished van der Waals forces of CNTs. Surface-decorated nVACNTs display an increased sensitivity to NO_2 gas, which is attributed to the enhanced quality of the reactive catalyst deposition and augmented permeability. This strategy achieves a larger decorated area while increasing a catalytically active reaction area. The obtained results promise that the enhanced nVACNTs will expand the industrial applications of carbon nanotubes.

1. Introduction

Vertically aligned carbon nanotubes (VACNTs) are used in various applications, such as physical/chemical/biological sensors,[1–5] field emission devices[6,7], transistors[8,9], adhesive[10,11], and energy storage systems,[12–15] owing to their outstanding mechanical properties, including a high tensile strength and elastic modulus,[16] an excellent chemical stability,[17] and desirable electrical characteristics, such as a high electrical conductance [18] and high specific surface area with porous structure[19]. Although the excellent alignment of VACNTs have contributed to their reliable performances in various applications,[20–22] their

abundant van der Waals forces and low mechanical resilience limit the deformation recovery of VACNTs upon the application of external forces.[23] Furthermore, their inherent chemical inertness resulting from a high crystallinity and purity has prompted efforts to impart functionality using various atomic decoration processes.[24,25] Consequently, various coating methods have been applied to enhance the functionality of VACNTs. However, it is well known that conventional liquid-based functionalization methods, such as spin coating, dip coating, and spray coating, are not suitable for preparing uniform coatings due to aggregation between the CNTs. This aggregation takes place because of the surface tension of the liquid, the low surface energy of the VACNTs, and the strong resistance of the VACNT nanostructures to liquids.[26,27] Therefore, atomic decoration methods, such as atomic layer deposition (ALD)[28–37] and electron-beam (E-beam) deposition[38–40] have been developed to functionalize VACNTs.

Recently, efforts have been made to enhance the mechanical elasticity and durability of the VACNT by applying ceramic thin films including zinc oxide (ZnO),[41] alumina (Al_2O_3),[41–43] and titanium dioxide (TiO_2)[44,45] via ALD. However, despite the application of the ALD process, the high density and aspect ratio of the VACNT result in low atomic penetration, ultimately preventing the formation of a uniform coating from the VACNT base to its tip apex.[42,46] Accordingly, the ceramic coatings tend to agglomerate on top of the VACNTs rather than generating uniform coatings on the individual CNT strands.[42,47] Equivalent limitations are observed in gas sensor applications utilizing VACNT. In VACNT-based gas sensors, sensitivity to detect harmful gases is enhanced by coating a reaction catalyst. Nevertheless, the reduced penetrability owing to the high VACNT density leads to degradation of the catalyst coating and a reduced reactivity. Moreover, the low atomic permeability of the VACNT structure hinders the deep penetration of gases, further limiting the potential detection capabilities of such systems.

To improve the atomic penetrability of the VACNT structure, ongoing efforts are focused on enhancing the uniformity of the atomic decoration. For example, microscale pattern modulation

has been applied to VACNTs to increase their penetrability.[48–50] The use of micropatterned VACNTs was found to result in a marginal enhancement in the gas permeability, thereby facilitating the penetration of ceramic atoms via the ALD approach. The micropatterns thereby allowed the uniform deposition of ceramic atoms around these pattern holes.[44] However, despite such advances, the atomic penetrability remained constrained in terms of the single CNT strands. The limitations of VACNTs with these micropatterns are also evident in gas sensor applications due to their partial restriction of enhanced atomic penetration. Although micropatterning can enhance the sensitivity of VACNT-based gas sensors by improving the catalytic coating and gas permeability, it can be argued that these improvements at the microscale fail to exploit the complete reactivity of the VACNTs.[49] To overcome these limitations, various research groups have attempted to develop nanopatterned VACNTs. Therefore, numerous researchers have endeavored to nanopatterned VACNT as a solution to these limitations. In this context, the chemical vapor deposition (CVD) process for the fabrication of high-purity VACNTs involves the distribution of Al_2O_3 and iron (Fe)-based seeds in the form of nanopatterns and in the absence of adhesives, such as organic materials.[51,52] However, the process constraints for VACNTs fabrication based on the CVD process hinders the applicability of the transfer, lithography, and imprinting methods that require the use of adhesives or polymers, thereby rendering the nanopatterning of VACNTs particularly challenging. Although previous research on the nanopatterning of VACNTs has been reported, the range of nanopattern geometries has been primarily limited to basic patterns such as line and pillar, and the precision of these nanopatterns at the nanoscale has been relatively insufficient. For example, the nanoscale line shapes of VACNTs were unintentionally curved rather than straight, and the circular patterned VACNTs exhibited non-uniform diameters and heights. Additionally, atypical and randomly oriented nanoscale VACNTs have also been reported as nanopatterned VACNTs.[53,54]

Thus, with the above considerations in mind, this research proposes highly uniform and precise nanopatterned VACNTs (nVACNTs) that are prepared using a seed nanostructuring approach, wherein the nanotransfer printing (nTP) technique is employed to achieve an enhanced atomic penetrability and improve the quality of atomic decoration. The proposed method, which is aimed at fabricating a nanopatterned VACNT seed layer without the use of adhesives, has the potential to increase the VACNT purity by reducing in-process contamination. Using this method, the fabrication of nVACNTs with diverse nanopatterns is realized, and two applications of the prepared nVACNTs are proposed. To observe the enhanced atomic decoration uniformity from the base to the tip apex, ALD is employed to achieve coating with ZnO and Al_2O_3. The atomic decoration uniformity of the resulting VACNTs is then analyzed by comparing the atomic penetration ratios of the micropatterned VACNTs and the nVACNTs in both the horizontal and vertical directions. A more uniform ALD coating would be expected to facilitate the application of nVACNTs in various mechanical applications that require improved resilience. Additionally, the potential of the nVACNTs to enhance the atomic decoration rates of physical vapor deposition techniques, such as E-beam deposition, is also verified. Furthermore, the NO_2 gas-sensing capability of the nVACNTs is found to be much greater than that of non-patterned VACNT.

2. Results and Discussion

In this study, we fabricated nanopatterned VACNTs (nVACNTs) and developed two different applications as illustrated in **Figure 1**. For facile fabrication of nVACNTs, we proposed transfer-based fabrication strategy to prepare the nanopatterned seed layer for VACNT growth, as shown in Figure 1a. The process initiates from depositing a gold (Au) film on a polyurethane acrylate (PUA) mold bearing nanopatterns that were generated using a nanoimprinting process (Figure S1a-c). Subsequently, the Au nanopatterns were transferred to a silicon (Si) wafer via oxygen (O_2) plasma treatment (Figure S1d). In this study, various nanopatterns were applied,

with the objective being the fabrication of VACNTs characterized by diverse nanopatterns, including line (width: 400 nm, pitch: 600 nm), square dots (width: 800 nm, pitch: 1000 nm), cross dots (width: 350 nm, pitch: 1600 nm), and cross holes (width: 350 nm, pitch: 1600 nm). Then, ~10 nm of Al_2O_3 layer and ~ 1 nm of Fe layer were sequentially deposited via E-beam deposition (Figure S1f-g), followed by a lift-off process removing the Au pattern (Figure S1h). The remained Al_2O_3/Fe nanopatterns served as the catalyst for the growth of VACNTs. We used thermal CVD to synthesize the multi-walled CNTs with diameters of 5-10 nm (Figure S1i), as detailed in **Figure S1**. Depending on the 2D shape of the transferred seed pattern, VACNTs can form 3D architectures with nanoscale vertical channels which facilitates the gas flow. More specifically, as shown in Figure 1b, ALD was employed to achieve a uniform atomic decoration of the entire VACNT strands owing to the enhanced atomic penetrability within nVACNTs. We coated ultrathin ceramic films on surfaces of the individual CNT fibers which can reduce their van der Waals forces (P_{vdw}) and enhance the mechanical resilience ($P_{recovery}$), therefore achieving a fully recoverable ultralight nanofoam, as depicted in Figure 1c-d. In addition, we deposited Au catalyst on the nVACNTs using E-beam deposition, as shown in Figure 1e, realizing a NO_2 gas sensor with an enlarged chemically-active surface area, as depicted in Figure 1f. To achieve superior performances on both applications, the uniform atomic decoration and improved gas permeability enabled by the nanoscale vertical flow channels were essential. Detailed information about the experimental procedures is explained in the Methods section.

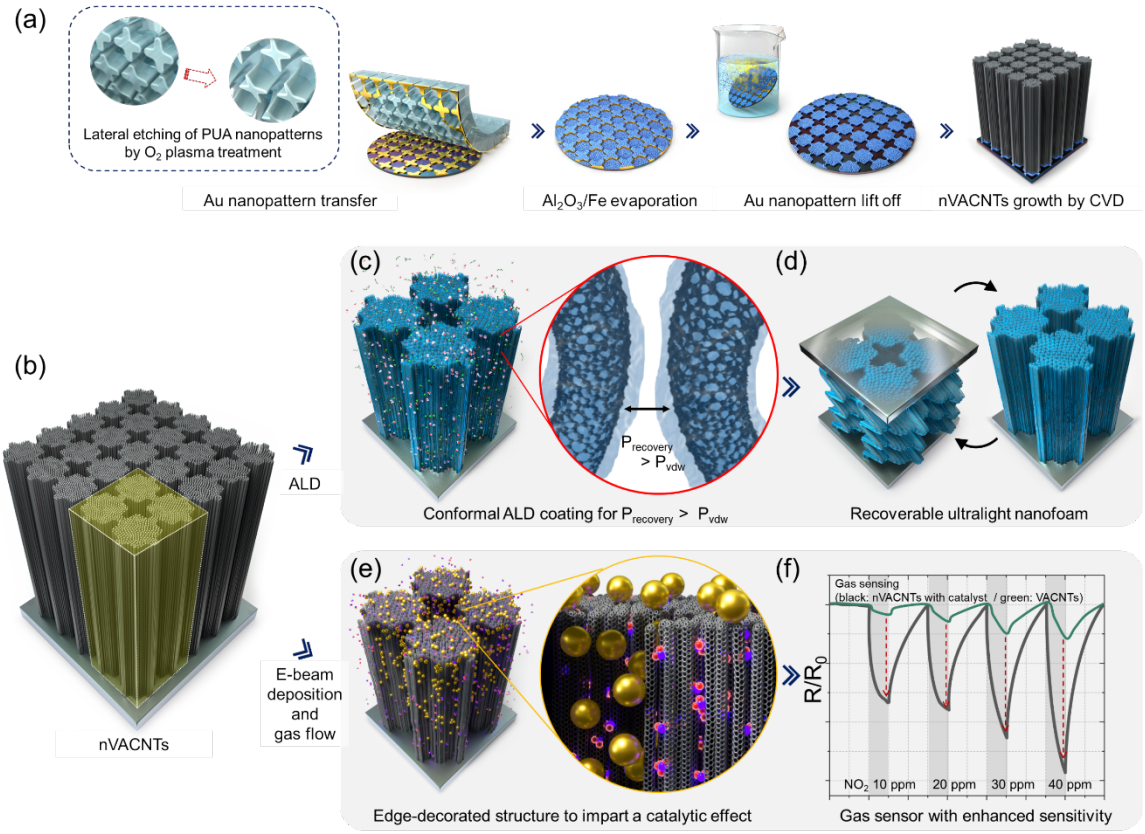

Figure 1. Schematic representation of the nVACNTs fabrication process and its applications. (a) Nanostructuring strategy schematic of nVACNT. Nanopattern imprinting process using PUA polymer is conducted for nVACNT seed nanopatterning. O_2 plasma is treated for etching PUA mold to enhance transfer quality. After plasma treatment, Au nanopatterns are transferred to the silicon (Si) wafer. Al_2O_3 and Fe are evaporated on Au nanopatterns transferred Si wafer. Then, the Au nanopattern is etched using the Au etchant and ultrasonication. nVACNT is grown by the CVD method. (b) Structural representation of the nVACNTs. (c) Schematic illustration of the atomic layer deposition (ALD) on nVACNTs (Blue color: ALD treated areas of functional materials (e.g., ZnO or Al_2O_3), violet and green color: ALD gas molecules). The atomic decoration causes a higher mechanical resilience ($P_{recovery}$) and a lower van der Waals forces (P_{VDW}). (d) The mechanical recovery of the VACNTs is enhanced by decoration with inorganic materials such as ZnO. (e) Schematic representation of the atomic decoration of the VACNTs by E-beam deposition (Gold color: metal (eg. Au) catalyst particles for gas sensors,

pink color: harmful target gas molecules). (f) Application of the Au catalyst-decorated VACNTs as a NO_2 gas sensor. Upon varying the concentration of NO_2, the resistance changes (black line: nVACNTs with catalyst, green line: VACNTs).

It was found that the bond between the PUA mold and the Au nanopattern (P_{mold}) was weakened following O_2 plasma etching of the mold, and activated hydroxyl groups were generated on the mold surface.[55,56] Surface treatment therefore enables covalent bonding between the Au nanopatterns and the target substrate ($P_{substrate}$) under the appropriate conditions, and prior research[57–59] has documented that a reduction in P_{mold} and an enhancement of $P_{substrate}$ facilitate Au nanopattern transfer.[55,60] To ensure stable transfer of the nanopattern, the condition presented in Eq. (1) must be met:

$$P_{substrate} - P_{mold} > 0 \quad (1)$$

A schematic representation of the PUA mold etching process is shown in **Figure S2**, and the effectiveness of this process was evaluated using scanning electron microscopy (SEM). As shown in **Figure 2**a-i, the Au nanopatterns on the PUA mold measured 610 nm prior to the transfer process. This figure also shows the result of the Au layer transfer to the Si wafer via the heat press method. In the absence of O_2 plasma treatment, the PUA mold did not undergo etching and form the hydroxyl group on the surface, thereby rendering it impossible to transfer the Au nanopattern onto the wafer without an adhesive due to low adhesion between the Au nanopatterns and the Si wafer surface. Thus, Figure 2a-ii shows that the transfer of Au nanopatterns to the Si wafer was not successful.

To overcome this poor transfer characteristics, O_2 plasma treatment was conducted for 20 min, leading to a reduction in the width of the PUA nanopatterns from 610 to 533 nm. This treatment resulted in a reduction in P_{mold} owing to side etching and an increase in $P_{substrate}$ through the generation of hydroxyl groups on the Au nanopattern, which assisted the covalent bonding on the Si surface during the thermal pressing process; this enabled the complete transfer of uniform

Au nanopatterns onto the Si wafers. As shown in Figure 2b-i, the Au nanopatterns remained intact even after the PUA nanopatterns were subjected to a side etching. The etching of the PUA mold through O_2 plasma reduces the bonding force between the nanopatterns and the PUA mold, thus facilitating the transfer process. As a result, the Au nanopattern morphology being successfully transferred onto the wafer. In addition, Figure 2b-ii shows photographic images of the Si wafers exhibiting successfully transferred Au nanopatterns. **Figures S3** and **S4** show the etching and transfer results, which varied depending on the duration of the O_2 plasma treatment. More specifically, following treatment for 10 min, the PUA mold underwent etching to a width of 587 nm, indicating that a longer etching time was required to ensure successful transfer onto the wafer. Furthermore, upon increasing the treatment time to 30 min and beyond, the PUA mold was over-etched to a width of 262 nm, resulting in excessive transfer of both the intended Au nanopatterns and the undesired Au pattern region onto the Si wafer. These results therefore confirm that O_2 plasma treatment weakens the adhesion between Au and PUA, allowing transfer to low-adhesion surfaces without the requirement for additional adhesives. By employing the inverse image of the transfer process as the seed layer pattern, nVACNTs with diverse nanopatterns were fabricated (i.e., lines, square dots, cross-dots, and cross-holes), as shown in the SEM images presented in Figure 2c. As shown in **Table S1**, each nanopattern has the following dimensions: the line widths and pitch are 400 nm and 600 nm each. Concerning square dots, they comprise squares measuring 800 nm in length, with a 1000 nm in pitch. The cross-dot pattern is designed by two vertically intersecting lines, each with a width of 350 nm, and a pitch of 1600 nm (a length of 600 nm from the center of the pattern to its edge). Further, cross hole patterns represent the inverse phase of the cross-dot configuration. In addition, the inset shows an image of the transferred mold, demonstrating the successful transfer of complex-shaped nanopatterns such as cross dot and cross hole patterns, in addition to simple nanoscale lines and squares. Moreover, it was found that VACNT growth conformed to the shape of the nanopatterned seed. As can be seen from the cross-sectional morphology of the fabricated

nVACNT (Figure 2d), the VACNTs grew vertically along the nanopattern in a uniform manner to give a superior nanopatterning quality. **Figure S5** shows the SEM images of the PUA mold with Au-deposited nanopatterns, the etched and remaining Al_2O_3/Fe nanopattern reverse phase, and the grown nVACNTs, while **Figure S6** confirms that these nVACNTs can be uniformly fabricated over a large area. Additionally, the nVACNT quality was confirmed by observing the G- (1580 cm^{-1}) and D-bands (1360 cm^{-1}) using Raman spectroscopy (**Figure S7**).

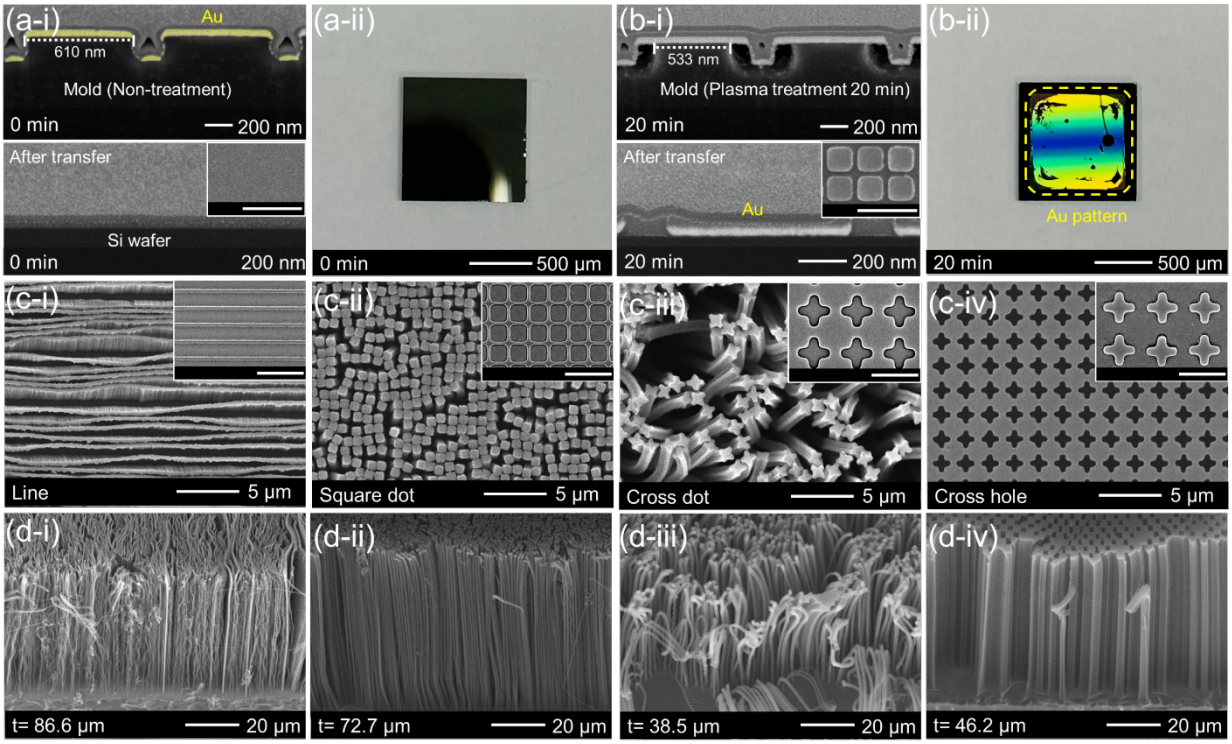

Figure 2. (a-i) Cross-sectional image of the Au-evaporated PUA mold without O_2 plasma treatment. Also shown is the Si wafer after the transfer process. (a-ii) Photographic image of the Si wafer after the transfer process (Inset image: Top view of Si wafer after nTP, scale bar: 1.5 μm). (b-i) Cross-sectional image of Au-evaporated PUA mold following O_2 plasma treatment for 20 min (Inset image: Top view of Si wafer after nTP, scale bar: 1.5 μm). After the transfer process, the Au nanopattern can be observed on the Si wafer. (b-ii) Photographic image of the Si wafer after the transfer process with O_2 plasma treatment. (c) top view SEM images of the nVACNTs (i: lines, ii: square dots, iii: cross dots, and iv: cross holes). Inset images shows

nTP results for nVACNTs fabrication (scale bar: 1.5 μm). (d) Cross-sectional SEM images of the nVACNTs (i: lines, ii: square dots, iii: cross dots, and iv: cross holes).

The vertically aligned yet spirally shaped CNTs with outstanding mechanical properties allow application of VACNTs as mechanical damping nanofoams with extreme energy dissipation and elastic recovery characteristics, as shown in **Figure S8**. Highly porous, ultralight VACNTs can achieve strength exceeding other established architected nanomaterials at similar low densities, such as ceramic nanolattices[61] and other carbon-based foams[62–65], and recover more than 97% compressive strain.6363 However, VACNTs require atomic surface decoration for self-recovery after externally induced compression. When a VACNT foam is extremely compressed more than ~10% of its original height, the vertically aligned individual CNT bundles will largely bend and buckle making multiple contacts with each other. Although the deformation of individual nanotubes may remain elastic under extreme deformation, the van der Waals force at nanoscale is strong enough to hold their compressed state preventing the elastic recovery. Therefore, a surface modification technique for surface energy reduction is necessary to engineer a highly recoverable VACNT. Extreme recovery of entire VACNT forest are enable only when all the CNTs can be uniformly coated by material with low intrinsic adhesive force such as ceramics. (e.g. ZnO, Al_2O_3) ALD is the most effective process for deposition of uniform layer on complex small structures, yet enabling the full penetration of oxidants and precursors into the nano-scale open-foamed VACNTs remains a challenge.[46,67] Ultimately, VACNT forests with modified surface properties for elastic recovery characteristic and high energy dissipation is limited in the size less than one square millimeter.

In case of non-patterned VACNTs, penetration of the precursors and oxidants into the structure during the ALD process is hindered owing to the dense structure of the VACNT array, **Figure 3**a. In case of micropatterned VACNTs (μVACNTs), introduction of micropatterns can improve the penetration of gaseous chemicals providing vertical gas flow channels, as shown in Figure

3b. However, the maximum penetration depth in lateral direction from the outside of vertical channels to the micro-structured array is only few micrometers or less,[46] therefore the deposition is limited on those inside the array structures. In contrast, nVACNTs can provide sufficient penetration channels to every CNT fiber, thereby maximizing the uniformity of the ALD coating, as depicted in Figure 3c. For verification, 100 cycles of ZnO ALD were carried out to the ~150 μm tall non-patterned, micropatterned, and nanopatterned VACNT forests. Both the micropattern and nanopattern have cross-shaped vertical channels with different scale and micropattern array has 10 times the size of the nanopattern array. The precursor and oxidant for ZnO ALD were diethylzinc and deionized water, respectively. After cutting the VACNT chip in half, the cross section of VACNT forest was observed by SEM, as shown in Figures 3d-3f. In addition, relative amounts of Zn were visualized via energy dispersive spectroscopy (EDS) for each case. In the case of the non-patterned VACNT, the amount of Zn decreases from top to bottom which indicates that vertical penetration of the oxidant and precursor molecules was insufficient. We derived the average Zn intensity according to the height via image processing of Zn EDS mapping images, as shown in Figure 3g, and quantitatively the EDS intensity at the bottom was reduced by 60% compared to the top surface. On the other hand, the ALD uniformity in the vertical direction significantly increased by introducing VACNTs with the vertical channels in patterned VACNTs. In both cases of μVACNTs and nVACNTs, the reduction in EDS the intensity along the vertical direction were remarkably small.

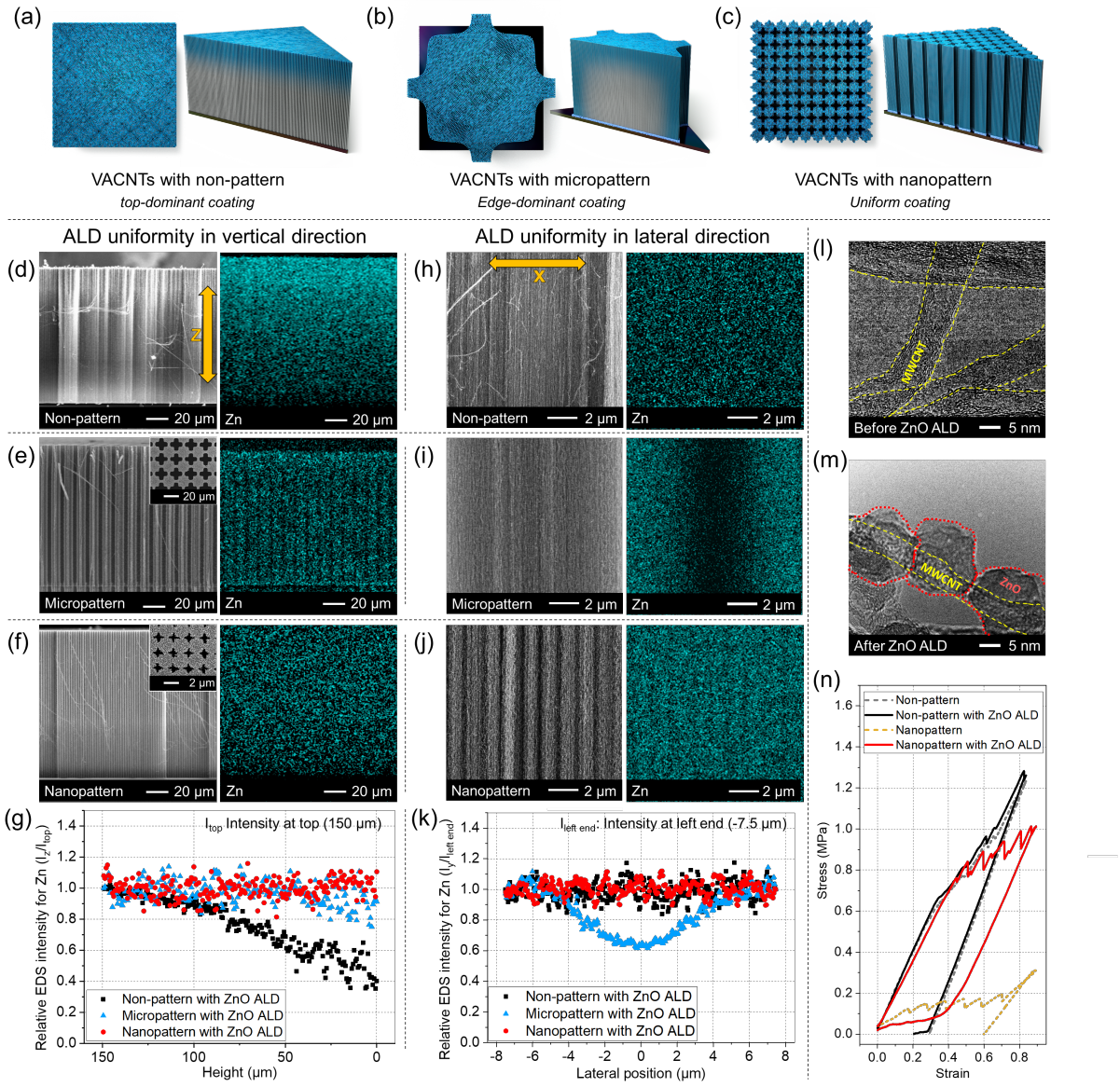

286

287 **Figure 3.** Enhancement of ALD uniformity by introduction of a nanopattern on VACNT and
288 its application as a nanofoam with elastic recovery characteristic and high energy dissipation.
289 Schematic illustration showing differences in deposition uniformity during the ALD process
290 for the (a) non-patterned VACNT, (b) μVACNT, and (c) nVACNT. Cross-sectional SEM
291 images and Zn EDS analysis results are shown for characterization of ZnO ALD uniformity in
292 vertical direction in the (d) non-patterned VACNT, (e) μVACNT, and (f) nVACNT. (g)
293 Relative Zn intensity according to the height, as derived by image processing of EDS mapping
294 images of Zn for various VACNTs after ZnO ALD. Cross-sectional SEM images and Zn EDS

analysis results are shown for characterization of ZnO ALD uniformity in horizontal direction in the (h) non-patterned, (i) μVACNT, and (j) nVACNT. (k) Relative Zn intensity according to the horizontal position, as derived by image processing. TEM images of individual CNTs from the nVACNT structure (l) before and (m) after ZnO ALD. (n) Strain–stress curves recorded for various VACNTs upon mechanical indentation to confirm enhanced penetration of gaseous chemicals by introducing a nanopattern, and its application to elastically recoverable nanofoam.

The lateral uniformity in ALD coating of the three different VACNT forests are shown in Figures 3h–3j, and the relative EDS intensity of Zn according to the horizontal position was derived by image processing of EDS mapping images for Zn in various VACNTs with ZnO ALD, as presented in Figure 3k. While non-patterned VACNTs and nVACNTs showed uniform Zn coating in lateral direction, the horizontal Zn intensity of μVACNTs was highly non-uniform. In terms of ZnO ALD quality along the horizontal axis, we indeed observe uniformity. However, upon considering the entirety of the non-patterned VACNTs area, we notice a significant decrease in atomic penetrability towards the bottom surface. The non-patterned VACNT exhibits a uniformly high ZnO coating ratio in the horizontal direction at the topmost region. However, as one descends in the vertical direction, a uniformly low ZnO coating ratio is observed due to the decreased atomic penetration. As the oxidant and precursor can flow through the vertical channels, CNTs near the perimeter of micropatterns along vertical direction are coated uniformly with ZnO. However, the reaction gas cannot sufficiently penetrate through the micrometer-width CNT array in lateral direction. Therefore, we observed only 60% of EDS intensity inside the micropattern compare to those near the perimeter. We compared our EDS mapping results of Zn and C and confirmed high uniformity of C in lateral direction of μVACNTs, as presented in **Figure S9**, which correspond with atomic analysis results presented for the various VACNTs in **Figure S10**. Such result implies that the low Zn intensity detected inside the μVACNTs is not caused by possible measurement obstruction but by the small

amount of Zn deposition. In contrast, the introduction of a nanopattern significantly reduced the required horizontal penetration depth. Although the EDS intensity for Zn was found to decrease in the same manner toward the center of the pattern, the reduction was only about 10%. It was confirmed that the ALD uniformity in the vertical direction was greatly improved by vertical channels that facilitate penetration of gaseous chemicals. In addition, by reducing the size of the pattern, it was possible to enhance the ALD uniformity in the lateral direction significantly as well as the uniformity in the vertical direction further. To verify that this advantage can be applied to other ALD processes, Al_2O_3 ALD was performed by changing the precursor. It was confirmed that the distribution of relative Al intensity from EDS map in nVACNT after Al_2O_3 ALD was similar to that for Zn in nVACNT with ZnO ALD, in both vertical and horizontal directions, as shown in **Figures S11**a-d. Meanwhile, to verify the coating uniformity at the nanoscale, the CNTs from the nVACNTs both before and after ALD were dispersed and observed at a high magnification. Figures 3l and 3m show the resulting transmission electron microscopy (TEM) images of the nVACNT before and after ZnO ALD, respectively, confirming the deposition of ZnO layer on the CNT surface.

Previously, it has been reported that ALD can be used to fine-tune the VDW forces and recovery forces between CNT pairs in a VACNT pillar tens of micrometers wide, which could then impart the VACNT micropillars with recovery characteristics during unloading through separation of the contacted CNT pairs.[66] To further verify the improvement in penetration of gaseous chemicals resulting from the introduction of a nanopattern, the size of the VACNT arrays, whose width and height were 25 μm or less due to the limited penetration of gases, was increased to a 1 cm × 1 cm scale with a height of ~100 μm. Subsequently, mechanical indentation by truncated cone tip made of titanium carbide was conducted on these VACNT forests both before and after ZnO ALD, and their mechanical behaviors were compared, Figure 3n. In order to match the strain rate and maximum strain as much as possible to 0.01 s^{-1} and 0.85, similar to the previous report,[66] the tip speed and indentation depth was fixed at 1 μm s^{-}

[1], and 85 μm, respectively. In the loading process, the nVACNT specimen without ALD exhibited a relatively low stiffness of 0.428 MPa at the initial slope, compared to the non-patterned VACNT without ALD that showed stiffness of 1.86 MPa. The low stiffness at initial slope of nVACNT is due to its smaller cross-sectional area. After the initial region of linear slope, rise and fall of stress are repeated as previously reported,[63,66] by progressive buckling of VACNTs. And then, densification of CNT occurs and the stress increase rapidly. The non-patterned VACNT and the nVACNT were indented with maximum strains of 0.835 and 0.891, respectively. In the unloading step, 65% and 33% of strain for non-patterned VACNT and nVACNT was elastically recovered. As a result, non-patterned VACNT and the nVACNT showed residual strain of 0.290 and 0.597, respectively. High residual strain above 0.25 in both VACNTs resulted from the CNT pairs entangled with each other by densification do not fall off again due to their high intrinsic adherence forces. After conducting ALD on non-patterned VACNT and nVACNT, the effect of ALD on the mechanical behavior of VACNTs differed dramatically depending on whether the nanopattern exists or not. Following 120 cycles of ZnO ALD, the stiffness at initial slope was significantly enhanced by 271% in the nVACNT specimen compared to that of the non-patterned one, which was enhanced by less than 5%. This was attributed to ALD taking place over the entire surface of the nVACNT, as opposed to only top-dominant deposition in the non-patterned VACNTs. Differences between non-patterned VACNT and nVACNT in stiffness change before and after ALD implies that the low stress inherent in nVACNT can be compensated by ALD, and that the increase in the number of ALD cycles will allow the stiffness of nVACNT to surpass that of non-patterned VACNT. The non-patterned VACNT and the nVACNT with ALD were indented with maximum strain of 0.836 and 0.893, respectively. In the unloading step, homogeneous ALD was found to be possible upon the introduction of nanopattern. As shown in the unloading curve of Figure 3n, in the case of non-patterned VACNTs, residual strain was slightly reduced from 0.290 to 0.205, showing a slight increase of the proportion for elastic strain to the total strain from 65% to 75%. On the

other hand, residual strain of nVACNTs was extremely reduced from 0.598 to zero, showing a fully elastic recovery after ALD. This is due to the fact that ALD is carried out throughout the CNTs by the introduction of nanopatterns, which significantly reduces the adhesion force on the surface of all CNT bundles, making them easy to separate from each other during the unloading process even after if CNTs adhere to each other once by the buckling and densification during the loading step. Ex-situ SEM images support the superb elastic recovery of nVACNTs with ZnO ALD. **Figure S12** shows the images after indentation of the non-patterned VACNT and nVACNT with ZnO ALD. Even after ZnO ALD, non-patterned VACNT shows insufficient recovery after indentation, as presented in Figure S12a and b. In contrast, nVACNT shows complete recovery. As shown in Figure 12c and d, nVACNT with ALD shows near-perfect recovery, except for the occurrence of an extremely small surface step, indicated by yellow arrows in Figure S12c-f, resulted from miss-alignment between the indenter and the surface of nVACNT. Meanwhile, from the perspective of energy dissipation, nVACNTs with ALD outperforms nonpatterned VACNTs. In the case of non-patterned VACNTs, the energy dissipation density in the indentation process before and after ALD is 230 kJ m^{-3} and 235 kJ m^{-3}, respectively, which increases by only 2% after ALD. On the other hand, in the case of nVACNTs, the energy dissipation density before and after ALD is 89.8 kJ m^{-3} and 279 kJ m^{-3}, respectively, which increases by 210% after ALD. It is notable that energy dissipation density of nVACNTs, which was 61% lower than non-patterned VACNTs before ALD, overwhelm non-patterned VACNTs after ALD. These results show that introduction of nanopatterns can be a solution for the limitation in the size of VACNTs, which was pointed out as a challenge to achieve homogeneous coating on VACNTs through ALD, and thus expands the utilization of VACNTs as a mechanical damping nanofoam with both elastic recovery characteristic and high energy dissipation.

It is therefore expected that penetration of gaseous chemicals can be enhanced in VACNT forests through the introduction of nanopatterns. The developed nVACNT material was subsequently employed as a NO_2 gas sensor to further investigate the effect of VACNT nanopatterning on gas-sensing applications. The importance of sensing toxic or pollutant gases (such as NO_2) for detecting and controlling pollution has increased in recent decades owing to their adverse effects on the environment and human health. VACNTs are considered promising candidates for gas sensing because of their high surface area-to-volume ratio, high electron mobility, high uniformity, good physicochemical stability, and high adsorption capability.[68] In addition, in recent decades, researchers have found that the sensing performance, including the sensitivity, can be further improved by decorating the VACNTs with various noble metal catalysts (e.g., Au and Pt), which could promote the commercialization of VACNT-based gas sensors.[69] However, as shown in **Figure 4**a-i, two significant challenges remain in the area of catalyst-decorated VACNT-based gas sensors, which can ascribed to the high density of VACNTs. More specifically, this high density hinders the penetration of the target gases into the deeper VACNT region, thereby limiting the reactions of target gases to only the top surface region. This results in a reduction in the active surface area of the VACNT and subsequently decreases the sensitivity of the sensor. Secondly, the high VACNT density prevents the deep penetration of noble metal atoms, limiting the catalytic effect. Typically, noble metal catalysts are coated on VACNTs through a physical vapor deposition (PVD) process; thus, they are decorated on only the top surface. It is therefore reasonable to expect that the developed atom-penetrable nVACNT material will overcome the aforementioned limitations and further enhance the sensing performances of VACNT-based gas sensors.

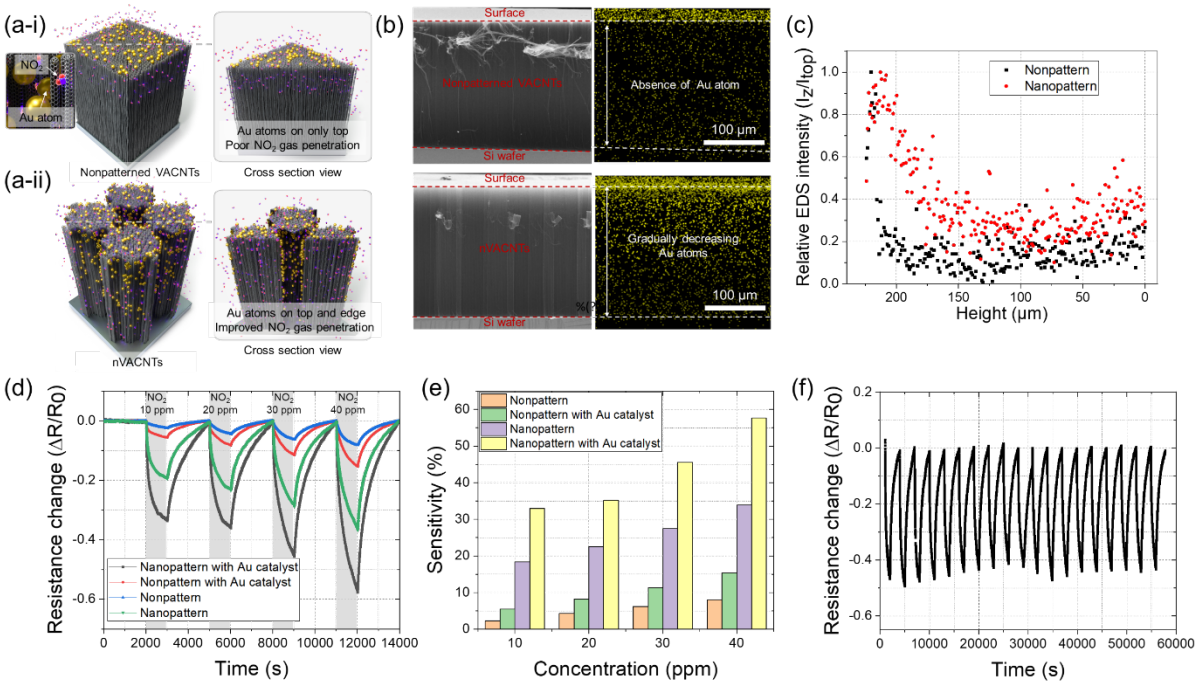

421

422 **Figure 4.** Application of the nVACNT material as a high-performance NO_2 gas sensor.
423 Schematic illustration of the gas sensors based on (a-i) Au-decorated non-patterned VACNTs
424 and (a-ii) Au-decorated nVACNTs and their corresponding sensing mechanisms. (b) Side-view
425 SEM and EDS images showing the Au-decorated non-patterned VACNT and nVACNT
426 materials. The yellow dots in the EDS images represent the Au atoms and indicate their
427 densities in the two materials. (c) Relative EDS intensities for the Au-decorated non-patterned
428 VACNT and the nVACNT at different height locations along the VACNTs. The intensity
429 corresponding to the yellow color (Au) was normalized based on the yellow dot intensity of the
430 top surface of each VACNT image. (d) Gas sensing results for the different gas sensors in the
431 presence of NO_2 gas at concentrations of 10, 20, 30, and 40 ppm, and (e) the corresponding
432 calculated sensitivity. (f) Gas cyclic test results for the sensor based on the Au-decorated
433 nVACNTs under repeated exposure to NO_2 gas (30 ppm) and air (80% N_2, 20% O_2).

434

435 As shown in Figure 4a-ii, the nanopatterning of VACNTs not only results in an increased active
436 surface area, but it also enables deeper catalyst decoration. More specifically, as discussed in

relation to Figure 3, gas molecules can freely penetrate the VACNTs in both the vertical and horizontal directions, allowing the entire surface area to interact uniformly with the target gas. Furthermore, during the PVD process, the evaporated catalyst atoms are able to travel through the nanosized holes, thereby enabling their deposition on the top and sidewalls of the nanopatterned CNT bundles. It is noteworthy that owing to the line-of-sight nature of the PVD process and the relatively large atom size, catalyst decoration inside the individual CNTs is not possible. As shown in Figure 4b, an E-beam evaporator was used to coat the Au catalyst on non-patterned CNTs, which resulted in the Au atoms being deposited on only the top surface. However, when nVACNTs were used, Au atoms were deposited in deeper regions. If the amount of catalyst coating on the top surface is normalized as $l_{z,\ top} = 1$, it was found that the catalyst amount gradually decreased as the depth increased for the nVACNT. In contrast, the catalyst amount decreased to zero in the case of the non-patterned VACNTs, as shown in Figure 4c. The sparsely distributed yellow dots in the EDS image of the non-patterned VACNT material indicate the relative absence of Au atoms, with an atomic percentage of Au close to zero.

As shown in Figure 4d, the gas-sensing performance of the VACNT material was investigated for NO_2 gas at concentrations of 10, 20, 30, and 40 ppm. Initially, the catalytic effects of Au on the sensing performance of the non-patterned VACNT material were assessed, revealing sensitivities that were 2.39, 1.90, 1.84, and 1.93 times higher in the presence of the Au catalyst at each gas concentration, respectively (Figure 4e). In addition, the nanopatterning effects of the VACNTs were evaluated, giving sensitivities that were 8.00, 5.23, 4.43, and 4.23 times higher than that of the Au-free VACNT system at each gas concentration, respectively. It was found that the nVACNT loaded with the Au catalyst demonstrated a remarkable improvement in sensitivity, with sensitivity that were 14.35, 8.19, 7.35, and 7.21 times higher than that of the Au-free VACNT system at concentrations of 10, 20, 30, and 40 ppm, respectively. This significant improvement in sensitivity can be attributed to the synergistic effects of the

increased active surface area and the improved uniformity of the decorated catalysts in the vertical direction. In conclusion, the nanopatterning of VACNTs clearly facilitated atomic penetration of the target gas and the catalyst, resulting in improved sensitivities with an excellent cyclic stability as shown in Figure 4f.

3. Conclusion

This study introduced an nTP approach based on adhesion force modulation between the nanoimprinted mold and the deposited target material, which enables the fabrication of nVANCTs. The use of surface modification by utilizing O_2 plasma and the lateral etching of the nanopatterned substrate eased the transfer of nanopatterns. This advancement addresses issues related to the downscaling of VACNTs patterns and CVD chamber contamination associated with polymer melting and adhesive usage in conventional nTP processes. This innovative technique can yield significant advantages, which include the enhancement of atomic penetration properties within the realm of nanoscale VACNTs patterning and atomic-decorated applications. As enhanced atomic permeability in nVACNTs maximized the effect of ALD, the ZnO ALD improved the energy dissipation density of nVACNTS by 210%, showing a significant difference from that of non-patterned VACNTs which was improved by only 2%. Moreover, the substantial enhancement in mechanical properties achieved through nVACNTs-based ALD processing can be attained on a 100 mm^2 scale in contrast to prior studies in which the size of the VACNT array was limited to less than 1 mm^2. In terms of gas-sensing applications, the enhanced deposition area of the Au catalyst and gas permeability, stemming from the improved atomic permeability of nVACNTs, led to a remarkable sensitivity improvement of up to 14.35 times when compared with that of the nonpatterned VACNTs. This marks a noteworthy advancement in the VACNTs field of recoverable energy dissipation nanofoam and sensitive gas sensor technologies.

Although the nanopatterns were exclusively transferred onto a Si wafer in this study, they are expected to be applied to various substrate materials, including glass and flexible substrates that can withstand the elevated temperatures necessary for nVACNTs synthesis. Moreover, the ALD technique is not limited to ZnO; hence, it can be applied to a variety of materials on nVACNTs, allowing for improved mechanical performance and the incorporation of desired functionality. In the gas sensing aspect, although only Au decoration and NO_2 gas sensing were demonstrated in this study to verify the synergistic effects of VACNT nanopatterning, nVACNT with versatile catalysts can be effectively utilized for various toxic or explosive gas sensing applications in subsequent research. Utilizing VACNTs with various precise nanopatterns is anticipated to streamline the atomic decoration of diverse materials or catalysts, meeting the specific requirements of multiple industries to achieve various functionalities. Consequently, this advancement is poised to broaden and boost the practical industrial application of nVACNTs.

4. Methods

Fabrication: Si master molds with various nanopatterns were fabricated through krypton fluoride lithography. The fabrication process began with photolithography, where a bottom anti-reflective coating layer of 58 nm thickness and a photoresist layer of 1.0 μm thickness were sequentially deposited onto the substrate. Subsequently, the substrate underwent a soft bake process at 100°C for 60 seconds followed by a post-exposure bake process at 110°C for 660 seconds. Afterward, the substrate was immersed in a developer solution for 60 seconds to remove the exposed regions of the photoresist. Next, the etching process was carried out using a mixture of gases, including Cl_2 with a flow rate of 30 sccm and HBr with a flow rate of 180 sccm, under a pressure of 12 mTorr and a power of 300 W. This step selectively etches the exposed areas of the Si substrate, resulting in the desired nanopatterned Si master mold.

Then, the master wafers comprising various nanopatterns were coated with a light-curable polymer, namely RM-311 polyurethane acrylate (PUA) resin (Minuta Technology Co., Ltd.,

Korea), to replicate the nanopatterns onto a silicon mold. After curing the nanopatterned PUA substrate by exposure to ultraviolet (UV) light, it was separated from the master wafer. Subsequently, a 30 nm-thick layer of Au was deposited onto the nanopatterned mold using an E-beam evaporator (Daeki Hi-Tech Co., Ltd., Korea). The surface was then subjected to O_2 plasma treatment to modify the surface energy and partially etch the nanopatterned PUA side for facile transfer of the Au nanopatterns onto the Si wafer without the requirement of an adhesive. These findings suggest that the increment of the $P_{substrate}$-P_{mold} contributes to the dependable transfer of nanopatterns. The Au nanopatterns were then transferred onto the wafer via thermal pressing at 60 ℃ and 5 bar pressure. Subsequently, an Al_2O_3 layer (10 nm thick) and a Fe layer (1 nm thick), which served as catalysts for VACNT growth, were deposited onto the wafer using an E-beam evaporator. The Au nanopatterns were selectively removed through Au etching using an Au etchant and ultrasonic wave treatment, leaving behind the nanopatterns. The VACNTs were then grown via thermal CVD to fabricate nVACNTs with the desired nanopatterns. This was achieved using a customized CVD furnace with a carbon-assisted VACNT growth protocol.[70,71] See **Figure S13** and **Table S2** for detailed description about experimental setup and recipe of the VACNT synthesis, respectively. The ALD of ZnO and Al_2O_3 was conducted using a customized thermal ALD reactor (ICOT Mini, ACOT).[72] The base pressure was below 30 mTorr, and the temperature of reaction chamber was set to 155 ℃ for ZnO ALD and 150 ℃ for Al_2O_3 ALD. Trimethylaluminum and diethylzinc were used as precursors for the ZnO and Al_2O_3 ALD processes, respectively. Deionized water and nitrogen were used as the oxidant and the carrier gas, respectively. One ALD cycle consisted of precursor feeding for 0.5 s, flowing of N_2 (3 sccm) for 25 s, vacuum pumping for 90 s, oxidant feeding for 0.5 s, flowing of N_2 (3 sccm) for 25 s, and vacuum pumping for 90 s.

Morphological and Elemental Analyses: The morphological characteristics of the nanopatterned VACNTs were analyzed using ultra-high-resolution SEM (UHR-SEM; Hitachi High-Technologies Corp.). Cross-sectional examinations of the ALD-coated nanopatterned

VACNTs were performed using UHR-SEM combined with EDS to verify the morphology and composition. Moreover, UHR-SEM and EDS were employed to investigate the morphology and penetration of the Au catalyst into the non-patterned and nanopatterned VACNTs following E-beam deposition. TEM imaging was carried out using a Tecnai G2 F30 S-Twin instrument (FEI). For TEM analysis, the samples were prepared by dispersing the as-grown or ALD-treated VACNTs in isopropyl alcohol and dropping them onto lacey carbon-supported copper grids. Furthermore, Raman spectroscopy (Horiba Jobin Yvon) was employed to detect and analyze the characteristic graphitic and defect bands in the prepared VACNT specimens.

Mechanical Indentation: To prepare the samples for mechanical indentation, the VACNTs were grown to a height of 100±15 μm on a 1 cm × 1 cm wafer chip, and 120 cycles of ZnO ALD were carried out as necessary. Mechanical indentation was performed using a tribometer (UMT Tribolab, Bruker), with a truncated cone indenter tip made of titanium carbide having a diameter of 450 μm and an inclination angle of 45°. During indentation, the tip speed was set to 1 μm s^{-1}, and a 1 s idle time was included between the loading and unloading phases.

Evaluation of the Gas Sensor Performance: The non-patterned VACNTs and nVACNTs were decorated with Au (10 nm) using an E-beam evaporator (Daeki HiTech Co., Ltd., Korea). Subsequently, non-patterned VACNTs, Au-decorated non-patterned VACNTs, bare nVACNT, and Au-decorated nVACNTs were applied as gas sensors. NO_2 sensing tests were conducted using a customized gas chamber at 150 °C, and the gas content was controlled using a mass flow controller. The NO_2 target gas was introduced into the gas chamber at the desired concentrations (10, 20, 30, or 40 ppm) by controlling the flow rates of the NO_2, O_2, and N_2 components. It should be noted here that the ratio of O_2 to N_2 was maintained similar to that of ambient air. During the gas sensing tests, the electrical resistance of the gas sensor was measured using a source meter (2635 B; Keithley Instruments, USA).

Acknowledgements

J.-H. Ha, I. Yang, J. Ahn contributed equally to this work. This work was supported by a National Research Foundation of Korea (NRF) grant funded by the Korean government (MSIT, No. 2021R1A2C3008742 and No. 2022R1A2C4002115); Multi-Ministry Collaborative R&D Program (Development of Techniques for Identification and Analysis of Gas Molecules to Protect against Toxic Substances) through the National Research Foundation of Korea (NRF) funded by KNPA, MSIT, MOTIE, ME, and NFA (NRF-2022M3D9A102361832); Basic Research Program of KIMM (Korea Institute of Machinery and Materials, NK248B) funded by KIMM; the Development Program of Machinery and Equipment Industrial Technology (20018235, Development of inline nano-imprinter for nano photonic device) funded by the Ministry of Trade, industry & Energy(MI, Korea); the KAIST UP Program. This work was also supported by "Regional Innovation Strategy (RIS)" through the National Research Foundation of Korea (NRF) funded by the Ministry of Education (MOE)(2021RIS-004).

Received: ((will be filled in by the editorial staff))
Revised: ((will be filled in by the editorial staff))
Published online: ((will be filled in by the editorial staff))

References

[1] X. Wang, A. Ugur, H. Goktas, N. Chen, M. Wang, N. Lachman, E. Kalfon-Cohen, W. Fang, B. L. Wardle, K. K. Gleason, *ACS Sens* **2016**, *1*, 374.
[2] B. M. Li, O. Yildiz, A. C. Mills, T. J. Flewwellin, P. D. Bradford, J. S. Jur, *Carbon N Y* **2020**, *168*, 673.
[3] F. Ghasemi, *Sci Rep* **2020**, *10*, 11306.
[4] J. Ahn, J. Gu, B. Hwang, H. Kang, S. Hwang, S. Jeon, J. Jeong, I. Park, *Nanotechnology* **2019**, *30,* 455707.
[5] S. J. Kim, J. hun Jeong, G. Ryu, Y. S. Eom, S. Kim, *Sens Actuators B Chem* **2024**, *399, 134861*.
[6] P. Andričević, X. Mettan, M. Kollár, B. Náfrádi, A. Sienkiewicz, T. Garma, L. Rossi, L. Forró, E. Horváth, *ACS Photonics* **2019**, *6*, 967.
[7] A. Thapa, Y. R. Poudel, R. Guo, K. L. Jungjohann, X. Wang, W. Li, *Carbon N Y* **2021**, *171*, 188.
[8] M. Kansal, S. C. Sharma, *In: 2022 IEEE International Conference on Nanoelectronics, Nanophotonics, Nanomaterials, Nanobioscience & Nanotechnology (5NANO). IEEE*, **2022**, p.1.
[9] M. Kansal, S. C. Sharma, *Appl Phys A Mater,* **2022**, *128*, 1.
[10] Z. Zhou, T. Gao, S. McCarthy, A. Kozbial, S. Tan, D. Pekker, L. Li, P. W. Leu, *Carbon N Y* **2019**, *152*, 474.

[11] X. Jin, H. Tan, Z. Wu, J. Liang, W. Miao, C. S. Lian, J. Wang, K. Liu, H. Wei, C. Feng, P. Liu, Y. Wei, Q. Li, J. Wang, L. Liu, X. Li, S. Fan, W. Duan, K. Jiang, *Nano Lett* **2019**, *19*, 6756.
[12] M. Oguntoye, M. Johnson, L. Pratt, N. S. Pesika, *ACS Appl Mater Interfaces* **2016**, *8*, 27454.
[13] Y. Qiu, G. Li, Y. Hou, Z. Pan, H. Li, W. Li, M. Liu, F. Ye, X. Yang, Y. Zhang, *Chemistry of Materials* **2015**, *27*, 1194.
[14] K. Evanoff, J. Khan, A. A. Balandin, A. Magasinski, W. J. Ready, T. F. Fuller, G. Yushin, *Advanced Materials* **2012**, *24*, 533.
[15] A. Gohier, B. Laïk, K. H. Kim, J. L. Maurice, J. P. Pereira-Ramos, C. S. Cojocaru, P. T. Van, *Advanced Materials* **2012**, *24*, 2592.
[16] R. H. Baughman, A. A. Zakhidov, W. A. De Heer, *Science (1979)* **2002**, *297*, 787.
[17] E. Van Hooijdonk, C. Bittencourt, R. Snyders, J. F. Colomer, *Beilstein Journal of Nanotechnology* **2013**, *4*, 129.
[18] M. B. Jakubinek, M. A. White, G. Li, C. Jayasinghe, W. Cho, M. J. Schulz, V. Shanov, *Carbon N Y* **2010**, *48*, 3947.
[19] G. Sun, H. Ren, Z. Shi, L. Zhang, Z. Wang, K. Zhan, Y. Yan, J. Yang, B. Zhao, *J Colloid Interface Sci* **2021**, *588*, 847.
[20] Y. Zeng, L. Ci, B. J. Carey, R. Vajtai, P. M. Ajayan, *ACS Nano* **2010**, *4,* 6798.
[21] B. L. Wardle, D. S. Saito, E. J. García, A. J. Hart, R. Guzmán De Villoria, E. A. Verploegen, *Advanced Materials* **2008**, *20*, 2707.
[22] R. Guzmán De Villoria, A. J. Hart, B. L. Wardle, *ACS Nano* **2011**, *5*, 4850.
[23] T. Hertel, R. E. Walkup, P. Avouris, *Phys Rev B* **1998**, *58*, 13870.
[24] K. L. Stano, M. Carroll, R. Padbury, M. McCord, J. S. Jur, P. D. Bradford, *ACS Appl Mater Interfaces* **2014**, *6*, 19135.
[25] L. Acauan, A. C. Dias, M. B. Pereira, F. Horowitz, C. P. Bergmann, *ACS Appl Mater Interfaces* **2016**, *8*, 16444.
[26] C. T. Wirth, S. Hofmann, J. Robertson, *Diam Relat Mater* **2008**, *17*, 1518.
[27] F. An, C. Lu, J. Guo, S. He, H. Lu, Y. Yang, *Appl Surf Sci* **2011**, *258*, 1069.
[28] J. S. Lee, B. Min, K. Cho, S. Kim, J. Park, Y. T. Lee, N. S. Kim, M. S. Lee, S. O. Park, J. T. Moon, *J Cryst Growth* **2003**, *254*, 443.
[29] L. S. Liyanage, D. J. Cott, A. Delabie, S. Van Elshocht, Z. Bao, H. S. Philip Wong, *Nanotechnology* **2013**, *24,* 245703.
[30] Y. C. Hsueh, C. C. Wang, C. Liu, C. C. Kei, T. P. Perng, *Nanotechnology* **2012**, *23*.
[31] A. A. Dameron, S. Pylypenko, J. B. Bult, K. C. Neyerlin, C. Engtrakul, C. Bochert, G. J. Leong, S. L. Frisco, L. Simpson, H. N. Dinh, B. Pivovar, *Appl Surf Sci* **2012**, *258*, 5212.
[32] S. Boukhalfa, K. Evanoff, G. Yushin, *Energy Environ Sci* **2012**, *5*, 6872.
[33] D. S. Kim, S. M. Lee, R. Scholz, M. Knez, U. Gösele, J. Fallert, H. Kalt, M. Zacharias, *Appl Phys Lett* **2008**, *93, 103108*.
[34] C. J. Hu, Y. H. Lin, C. W. Tang, M. Y. Tsai, W. K. Hsu, H. F. Kuo, *Advanced Materials* **2011**, *23*, 2941.
[35] A. Gomathi, S. R. C. Vivekchand, A. Govindaraj, C. N. R. Rao, *Advanced Materials* **2005**, *17*, 2757.
[36] A. Javey, H. Kim, M. Brink, Q. Wang, A. Ural, J. Guo, P. Mcintyre, P. Mceuen, M. Lundstrom, H. Dai, *Nat Mater* **2002**, *1*, 241.
[37] Y. S. Min, E. J. Bae, K. S. Jeong, Y. J. Cho, J. H. Lee, W. B. Choi, G. S. Park, *Advanced Materials* **2003**, *15*, 1019.
[38] Q. H. Meng, C. Hao, B. Yan, B. Yang, J. Liu, P. K. Shen, Z. Q. Tian, *Journal of Energy Chemistry* **2022**, *71*, 497.
[39] T. F. Hsieh, C. C. Chuang, Y. C. Chou, C. M. Shu, *Mater Des* **2010**, *31*, 1684.

[40] H. Goktas, N. Lachman, E. Kalfon-Cohen, X. Wang, S. Torosian, K. K. Gleason, B. L. Wardle, *Nano Futures* **2023**, *7,* 025001.
[41] G. A. Malek, E. Brown, S. A. Klankowski, J. Liu, A. J. Elliot, R. Lu, J. Li, J. Wu, *ACS Appl Mater Interfaces* **2014**, *6*, 6865.
[42] K. L. Stano, M. Carroll, R. Padbury, M. McCord, J. S. Jur, P. D. Bradford, *ACS Appl Mater Interfaces* **2014**, *6*, 19135.
[43] L. Rovinsky, B. K. Barick, E. Lieberman, E. S. Avraham, G. D. Nessim, T. Segal-Peretz, N. Lachman, *ACS Appl Nano Mater* **2021**, *4*, 322.
[44] H. Zhang, B. Wang, B. Brown, *Appl Surf Sci* **2020**, *521,* 146349.
[45] L. Acauan, A. C. Dias, M. B. Pereira, F. Horowitz, C. P. Bergmann, *ACS Appl Mater Interfaces* **2016**, *8*, 16444.
[46] N. Yazdani, V. Chawla, E. Edwards, V. Wood, H. G. Park, I. Utke, *Beilstein Journal of Nanotechnology* **2014**, *5*, 234.
[47] G. J. Yuan, J. F. Xie, H. H. Li, H. L. Lu, Y. Z. Tian, *Coatings,* **2019**, *9,* 806.
[48] M. Yilmaz, S. Raina, S. H. Hsu, W. P. Kang, *Mater Lett* **2017**, *209*, 376.
[49] M. R. Mohd Asyraf, M. M. Rana, T. Saleh, H. D. E. Fan, A. T. Koch, A. Nojeh, K. Takahata, A. B. Suriani, *Fullerenes Nanotubes and Carbon Nanostructures* **2016**, *24*, 88.
[50] M. Microarchitectures, V. A. C. Nanotubes, D. Applications, *ACS Nano* **2011**, *5*, 994.
[51] S. Esconjauregui, M. Fouquet, B. C. Bayer, C. Ducati, R. Smajda, S. Hofmann, J. Robertson, *ACS Nano* **2010**, *4*, 7431.
[52] N. Yang, S. K. Youn, C. E. Frouzakis, H. G. Park, *Carbon N Y* **2018**, *130*, 607.
[53] A. Corletto, J. G. Shapter, *Adv. Sci.* **2021***, 8,* 2001778.
[54] I. Y. Y. Bu, V. Eichhorn, K. Carlson, P. Boggild, S. Fatikow, *Physica Status Solidi (A) Applications and Materials Science* **2011**, *208*, 2352.
[55] J. Ahn, J. H. Ha, Y. Jeong, Y. Jung, J. Choi, J. Gu, S. H. Hwang, M. Kang, J. Ko, S. Cho, H. Han, K. Kang, J. Park, S. Jeon, J. H. Jeong, I. Park, *Nat Commun* **2023**, *14,* 833.
[56] J. Ahn, J. Gu, Y. Jeong, J. H. Ha, J. Ko, B. Kang, S. H. Hwang, J. Park, S. Jeon, H. Kim, J. H. Jeong, I. Park, *ACS Nano* **2023**, *17*, 5935.
[57] S. Bok, G. H. Lim, B. Lim, *Journal of Industrial and Engineering Chemistry* **2017**, *46*, 199.
[58] Z. J. Zhao, J. Ahn, S. H. Hwang, J. Ko, Y. Jeong, M. Bok, H. J. Kang, J. Choi, S. Jeon, I. Park, J. H. Jeong, *ACS Nano* **2021**, *15*, 503.
[59] Z. J. Zhao, J. Ahn, D. Lee, C. B. Jeong, M. Kang, J. Choi, M. Bok, S. Hwang, S. Jeon, S. Park, J. Ko, K. S. Chang, J. W. Choi, I. Park, J. H. Jeong, *Nanoscale* **2022**, *14*, 1136.
[60] Y. Jung, J. Ahn, J. S. Kim, J. H. Ha, J. Shim, H. Cho, Y. S. Oh, Y. J. Yoon, Y. Nam, I. K. Oh, J. H. Jeong, I. Park, *Small Methods* **2022**, *6,* 2200248.
[61] L. R. Meza, S. Das, J. R. Greer, *Science (1979)* **2014**, *345*, 1322.
[62] P. D. Bradford, X. Wang, H. Zhao, Y. T. Zhu, *Carbon N Y* **2011**, *49*, 2834.
[63] S. Pathak, E. J. Lim, P. Pour Shahid Saeed Abadi, S. Graham, B. A. Cola, J. R. Greer, *ACS Nano* **2012**, *6*, 2189.
[64] K. H. Kim, Y. Oh, M. F. Islam, *Nat Nanotechnol* **2012**, *7*, 562.
[65] A. Misra, J. R. Raney, L. De Nardo, A. E. Craig, C. Daraio, *ACS Nano* **2011**, *5*, 7713.
[66] S. J. Park, J. Shin, D. J. Magagnosc, S. Kim, C. Cao, K. T. Turner, P. K. Purohit, D. S. Gianola, A. J. Hart, *ACS Nano* **2020**, *14*, 8383.
[67] S. M. George, *Chem Rev* **2010**, *110*, 111.
[68] T. Han, A. Nag, S. Chandra Mukhopadhyay, Y. Xu, *Sens Actuators A Phys* **2019**, *291*, 107.
[69] M. Penza, R. Rossi, M. Alvisi, E. Serra, *Nanotechnology* **2010**, *21,* 105501.
[70] N. T. Dee, J. Li, A. Orbaek White, C. Jacob, W. Shi, P. R. Kidambi, K. Cui, D. N. Zakharov, N. Z. Janković, M. Bedewy, C. A. C. Chazot, J. Carpena-Núñez, B. Maruyama, E. A. Stach, D. L. Plata, A. J. Hart, *Carbon N Y* **2019**, *153*, 196.

[71] J. Li, M. Bedewy, A. O. White, E. S. Polsen, S. Tawfick, A. John Hart, *Journal of Physical Chemistry C* **2016**, *120*, 11277.
[72] I. Yang, J. hun Jeong, J. Y. Seok, S. Kim, *Adv Energy Mater* **2023**, *13, 2202321*.